RSC Advances

PAPER

View Article Online
View Journal | View Issue

Cite this: *RSC Adv.*, 2026, **16**, 6595

Catalytic hydrothermal upcycling of end-of-life automotive plastic waste in near-supercritical water: process optimization and product characterization

Emmanuel Galiwango, * James Butler, Weiguo Ma, Kevin Austin and Samira Lotfi

This study investigates the catalytic hydrothermal conversion of heterogeneous end-of-life automotive shredder residues (ASR) waste in near-supercritical water, focusing on process optimization, thermodynamic behavior, and multi-phase product characterization. Factorial screening identified temperature and residence time as critical parameters, with 350 °C and 90 minutes yielding maximum hydrochar through enhanced carbonization and repolymerization, accompanied by reduced liquid yields and CO_2-rich gas production. Thermodynamic analysis revealed significant increases in water ionization constant (K_w) during non-isothermal heating, peaking at 1.44×10^{-12} mol^2 kg^{-2} at 350 °C, while density decreased to 0.619 g cm^{-3} under autogenous pressure. Isothermal reactions at 350 °C exhibited highly exothermic behavior ($\Delta H \approx -143$ kJ mol^{-1}) and strong ordering effects, correlating with peak hydrochar and gas yields. Catalyst screening demonstrated Ni-based catalysts' superior selectivity for phenolics and aromatic amines in the oil-phase, increased aqueous-phase total organic carbon, and minimized tar formation. Ru/Al_2O_3 favored ketone production, while non-catalyzed runs produced a broad range of C_6–C_{29} oil products and 341 g (CO_2)/kg(feed) as the only gas product. The optimized NiSiAl catalyst yielded a maximum hydrochar of 64.4 wt% with enhanced thermal stability (onset degradation ~425 °C), higher calorific values at 5 wt% feedstock concentration and feedstock-to-catalyst ratio of 9. The highest H_2 production (5 g kg^{-1} feed) occurred at a catalyst ratio of 5, while the best liquid yield (36%) was achieved at the lowest ratio of 1. The GC-MS analysis revealed feedstock concentration influenced reaction pathways, shifting from phenolics and amines at low solids loading to hydrocarbons and ketones at higher concentrations. These findings highlight catalytic hydrothermal conversion as a viable circular-economy route for ASR valorization, combining thermodynamic efficiency with targeted fuel and chemical production.

Received 15th December 2025
Accepted 25th January 2026

DOI: 10.1039/d5ra09706a

rsc.li/rsc-advances

1. Introduction

The global market value of automotive plastics was $28.1 billion in 2020 and is projected to increase to about $37 billion by 2028.[1] The shift from metals to increased use of plastics and composite materials continues to reshape the automotive industry due to advantages such as light weight, corrosion resistance, ease of processing, cost-effectiveness, and safety.[2,3] Renewable-powered vehicles, including electric vehicles (EVs), have contributed to the growth in vehicle production and increased plastic use in both hybrid and conventional vehicles. However, the attempt to solve fossil fuel-based environmental challenges may accelerate plastic pollution in the automotive industry especially when vehicles reach their end-of-life (EOL) or decommissioning stage.[4] One study suggested that even before EOL, plastic composite-containing vehicles with light weight that have covered about 132 000 km posed a negative environmental impact.[5]

The conventional EOL vehicle recycling focuses on recovering valuable metals, with the remaining components shredded into automotive shredder residue (ASR).[6,7] ASR contains a highly heterogeneous mixture of plastic polymers and hazardous substances, making recycling difficult due to low value and high treatment costs, leading to landfill disposal.[8–11] The growing ASR accumulation, stricter waste regulations, and environmental advocacy have prompted the automotive industry to explore sustainable management options.[12] Some countries like Japan consider ASR as hazardous waste due to the high content of heavy metals contained therein, thus, ASR has attracted more attention for sustainable treatment approaches.[13]

ASR is rich in carbon and hydrogen, offering significant energy potential that can be recovered through circular

Clean Energy Innovation, National Research Council of Canada, Ottawa, ON, K1A0R6, Canada. E-mail: emmanuel.galiwango@nrc-cnrc.gc.ca; Tel: +1 343-990-7709

economy approaches.[14,15] Thermal conversion approaches such as incineration, combustion and pyrolysis have been used to reduce waste and recover energy,[16–19] but these methods often generate pollutants due to halogenated additives and heavy metals.[20,21] Apart from incineration, thermochemical conversion route coupled with feedstock pre-treatment or product post treatment processes is widely considered as a viable alternative for upcycling ASR.[22,23] Pyrolysis is one of the most extensively studied thermochemical techniques for converting ASR into high-value products. Harder and Forton published a critical review of ASR pyrolysis developments, identifying key operational parameters such as temperature (500–850 °C), residence time, and feed composition as crucial for process optimization.[24] The review highlighted that the ASR pyrolysis can be tailored to maximize gaseous products since the production of oils or liquid fuels would require large space and high capital investment for the additional distillation plant. The ASR pyrolysis char contains high levels of metals, which can be repurposed in the cement industry where ASR char is generally excessive.[25,26] Despite these advantages, large-scale ASR pyrolysis has received limited attention due to chlorine contamination. During ASR pyrolysis, chlorine compounds were reported to corrode reactors, equipment liners, leading to higher operation costs and environmental risks.[27] In addition, chlorine affects pyrolysis products such as the decreased char reactivity, thus, lowering the char quality and economic value.[28] Moreover, ASR plastics contain other contaminants like halogens (Br) used as flame retardants in cars. During pyrolysis, these halogenated compounds breakdown into dioxins and persistent organic pollutants (POPs).[16] Catalysis is primarily used to improve the quality of pyrolysis products. For instance, zeolite catalysts reportedly improved carbon concentration in the char, and reduced organic contaminants in the ASR oil.[29] However, zeolites are prone to coke formation and deactivation challenges, and there are limited studies on ASR dichlorination.

In contrast, hydrothermal conversion offers a cleaner and potentially more efficient route. *In situ* dichlorination *via* hydrothermal conversion might be an interesting option since PVC, the main chlorine carrier in ASR can be dissolved at subcritical water and chlorine transferred as soluble chloride salts, hence, produce chlorine-free products like oil.[30,31] Application of catalysts such as nickel, accelerated hydrothermal dichlorination efficiency of PVC up to 87%.[32] Other studies reported the potential reduction of other pollutants in e-waste using hydrothermal conversion. For instance, Li and team published a review on hydrothermal treatment of per- and polyfluoroalkyl substances (PFAS), reporting >99% degradation and >60% defluorination of PFAS. The review recommended further studies beyond PFAS precursors but rather real-world waste streams and product characterization to elucidate on reaction kinetics and thermodynamics.[33] Nickel-based catalysts are stable in supercritical water, and titanium alloys were reported to deter corrosion and hydrothermal-induced equipment failures.[34,35] However, the cost of titanium (Ti) would make ASR commercial scale up adoption cost ineffective. Thus, using Ti-based catalyst precursor in stainless steel and cheaper alloys will likely reduce the equipment cost. Therefore, there is a literature gap on catalytic hydrothermal optimization and products characterization for a real-world complex waste stream like ASR at near-supercritical water to achieve complete degradation of the different type polymer plastics.

Hydrothermal conversion has emerged as a viable thermochemical technology for processing complex feedstocks such as plastics, wet heterogeneous wastes, and hazardous materials by utilizing water's physicochemical properties near or above its critical point.[36,37] This process enables efficient solubilization of organics and precipitation of inorganics, facilitating waste-to-energy and product recovery.[38,39] Although still in early industrial development, hydrothermal conversion shows promise for sustainable treatment and valorization of various feedstocks.[40,41] Hydrothermal processes are commonly classified as carbonization, liquefaction, or gasification.[42,43] However, focusing on one subdivision can misrepresent by-products as waste. For instance, many researchers reported optimal hydrothermal carbonization temperature in the range of 180–280 °C.[44–46] However, complex feedstocks such as ASR whose plastic fractions such as polypropylene and polyethylene (PP, PE), have degradation temperature above 300 °C and thus, are difficult to carbonize using most literature defined temperature range.[47] To address this, hydrothermal conversion incorporating catalysis at 350 °C has been redefined to promote near-supercritical reactions for complex plastic feedstocks.[48] This study extends that work by optimizing multiple parameters and catalyst systems for converting automotive fluff (AF) or ASR into low-carbon fuels and high-value products.

2. Materials and methods

2.1. Material preparation

Automotive fluff waste was collected from Quebec, Canada. Catalysts were purchased from Sigma-Aldrich (USA) and used without pretreatment. The highly heterogeneous AF waste contained hard plastics, rubber, sponge, wood, fines, *etc.*, as shown in Fig. 1 and was sorted prior to size reduction to remove larger inorganic particles such as glass, stones, metals that could damage the knife mill. In addition, the feedstock was soaked in water overnight to reduce ash content and sedment the fine, hard-to-mill materials. All AF fractions were then combined and shredded together in a SM 100 knife mill grinder (Retsch, Germany) to an average particle size of less than 1 mm, which was used for the characterization and hydrothermal reaction processes. The hydrothermal reactions were performed in a dedicated 4570 fixed head and a movable 250 mL-sized Inconel-T model vessel reactor (Parr instruments, USA). The system was equilibrated with 48 atm argon at 20 °C under constant stirring prior to the start of heating, to ensure no leak and inert reaction media. The reactor was heated from room temperature (20 °C) at an average non-isothermal heating ramping of 5.5 °C min^{-1} to achieve an isothermal set reaction temperature, and maintained there for a specified time. Parameter screening of reaction temperatures (230, 260 and 290 °C) and time of 30, 60 and 90 minutes were investigated. The reactor assembly schematic details were published in the previous study.[48]

Fig. 1 Picture of main components making up AF ground waste feedstocks.

2.2. Materials characterization

Feedstock and product fractions were characterized for thermal stability using thermogravimetric analysis, (TGA, Q5000 series, TA Instruments, USA). Following equilibration at 30 °C for 5 minutes, the samples were pyrolyzed at 20 °C min^{-1} to 900 °C under inert N_2 flow at 20 mL min^{-1}. The thermal decomposition profiles of weight as a function of temperature and time were continuously recorded and processed using TRIOS software (TA instruments). Elemental composition was analyzed using a CHNS analyzer (Elementar Vario EL cube, Germany). The carbon in the aqueous phase after reaction was analyzed using a total organic carbon analyzer coupled with a total nitrogen measurement unit (TOC-L CSH, TNM-L, Shimadzu, Japan). The changes in functional groups were studied using Fourier Transform Infrared Spectroscopy, Nicolet 6700 FT-IR instrument (Thermo scientific, USA). The spectra analysis on solid samples were performed within the range of 4000–500 cm^{-1} wavelength using 16 scans and 4 cm^{-1} resolutions. Additional analyses included; Brunauer–Emmett–Teller (BET) (ASAP 2020 series micromeritics, USA), and scanning electron microscopy-energy dispersive X-ray (SEM-EDX) SU5000 Hitachi SEM (Hitachi, Japan and Oxford instruments, USA). Gaseous and organic liquid products were analyzed using 8890A gas chromatography (GC) and the 7890A GC-5975C inert XL mass spectrum detector (Agilent technologies, USA), respectively. The details of the experimental set up and characterization procedures were published in the previous study.[48]

2.3. Calculations

The percentage yield of hydrochar or solid product (Y_{HS}) in eqn (1) was obtained as a weight ratio of product (M_{HS}) to AF feedstock (M_{AF}) loaded to the reactor on a dry basis.

$$Y_{HS} = \frac{M_{HS}}{M_{AF}} \times 100 \quad (1)$$

The percentage volumes of individual gas products analyzed through an off-line GC were converted to their respective mass. The total gas yield in eqn (2) was obtained as ratio of sum of weight ratio of gas products (M_G) to AF feedstock (M_{AF})

$$Y_g = \frac{\sum_i M_g}{M_{AF}} \times 100 \quad (2)$$

The percentage yield of the liquid products was determined according to eqn (3).

$$Y_l = 100 - (Y_{HS} + Y_g) \quad (3)$$

Estimation of energy recovery was determined from the high heating values of solid (HHV_{HS}) and gas products (HHV_{gas}) in MJ kg^{-1} were calculated using elemental analysis, ash and gas composition results using mathematical correlations as shown in eqn (4) and (5).[49] The energy and carbon recovery of the hydrochar were estimated according to eqn (6) and (7).[50]

$$HHV_{HS} = 3.49 \times \%C + 11.78 \times \%H + \%S - 1.03\%O - 0.15 \times \%N - 0.21 \times \%Ash \quad (4)$$

$$HHV_{gas} = 141.7 \times \%H_2 + 55.5 \times \%CH_4 + 51.9 \times \%C_2H_6 + 50.4 \times \%C_3H_8 \quad (5)$$

$$\text{Energy recovery}(\%) = \frac{HHV_{HS} \times M_{HS}}{HHV_F \times M_F} \times 100 \quad (6)$$

$$\text{Carbon recovery}(\%) = \frac{\%C_{HS} \times M_{HS}}{\%FC_F \times M_F} \times 100 \quad (7)$$

where HHV_F, M_{HS}, M_F, $\%C_{HS}$, and $\%FC_F$ are the high heating values of feedstock, mass of hydrochar, mass of feedstock, percentage of carbon and fixed carbon, respectively.

The ionic product and thermodynamic properties (enthalpy (ΔH), Gibbs free energy (ΔG) and entropy (ΔS)) of water products

at experimental temperatures and pressures were calculated using Marshall and Franck's empirical function.[51]

3. Results and discussion

3.1. Physicochemical properties

Table 1 shows the proximate, ultimate analysis and the surface properties of the feedstock and corresponding hydrochars of different reaction conditions. Proximate analysis results revealed elevated ash content and decreased volatile matter in all hydrochars. This was plausibly due to the elevated concentration of the inorganic materials such as metals and minerals in the automotive fluff as a result of conversion of the organic volatiles into carbonaceous products.[52] The elevated high ash content in Ti-based catalyst can be attributed to hydrothermal structural evolution of titanium dioxide enabling enhanced crystallization in form of ash.[53] Thus promoting An increase in feedstock concentration increased ash content and decreased volatile matter owing to increased inorganic content and extensive thermal decomposition causing polymerization reactions, respectively. Catalyst-based hydrothermal processing produced hydrochars with lower carbon content and high heating values compared to non catalyst upcycling. The observed improved energy recovery across increasing feedsctock concentration in NiSiAl-catalyzed reactions was attributed to the enhanced carbon content and the higher calorific value, that enabled feedstock valorization into more uniform (surface area) and stable products.

3.2. Product analysis

3.2.1 Hydrothermal parameter screening. Reaction temperature and residence time are critical parameters for hydrothermal conversion of different feedstocks to various products. Two-factor, 3 level factorial design of experiment was performed to investigate the effect of temperature and time on solid, liquid and gas yields as the response variables. As shown Fig. 2(A and B), hydrochar yield increased with both reaction time and temperature. In addition, the time–temperature interactions revealed that carbonization increased in order of 90 > 60> 30 minutes and 350 > 305 > 260 °C, respectively. The increased hydrochar yield was attributed to the increased thermal kinetics that favors repolymerization reactions of the organic components in the liquid phase.[54] Moreover, following the depolymerization of the feedstock to yield the observed initial high liquid monomers, the liquid yield as shown in Fig. 2(C and D) decreased in similar trend to that of hydrochar. The liquid yield reduction can be attributed to improved conversion rates of water-soluble organics towards gas phase.[55] Similar results of higher solid yield and reduced liquid product were reported in a study of simulated municipal solid waste containing PE, PET and pistachio hull.[56] The gas yield shown in Fig. 2(E and F) increased with temperature for 1 hour of reaction, owing to thermal cracking of the feedstock and the formed liquid product. However, when isothermal reaction time was increased from 60 to 90 minutes, the mean gas yield reduced by 1.5 from 4.8 wt%, plausibly due to the fractionation of the condensable gases back to liquid and eventually hydrochar. Noteworthy, the hydrothermal valorization achieved at 350 °C,

Table 1 Physicochemical analysis of hydrochar produced at different conditions[a]

		Hydrochar					
		NiSiAl-at feedstock concentrations (wt%)					
Properties	Raw ASR	No catalyst	5	10	20	Ru	Ti
Proximate analysis (%)							
Ash	40.03 ± 0.52	75.07 ± 0.20	72.89 ± 0.12	73.53 ± 0.52	78.17 ± 0.02	67.78 ± 0.12	84.83 ± 0.42
VM	38.43 ± 0.24	21.77 ± 0.20	25.92 ± 0.40	24.89 ± 0.22	19.21 ± 4.60	30.51 ± 0.10	13.57 ± 0.1
FC	21.54 ± 0.20	2.15 ± 0.04	1.73 ± 0.02	1.58 ± 0.24	1.65 ± 0.04	1.70 ± 0.02	1.20 ± 0.1
Ultimate analysis (%)							
C	32.40 ± 2.00	16.06 ± 2.66	9.32 ± 1.20	10.3 ± 0.85	14.46 ± 2.58	8.96 ± 2.70	4.87 ± 1.02
H	3.95 ± 0.20	2.03 ± 0.10	1.93 ± 0.19	2.23 ± 0.10	2.15 ± 0.38	1.76 ± 0.16	1.47 ± 0.08
N	0.82 ± 0.0	0.47 ± 0.07	0.27 ± 0.01	0.19 ± 0.02	0.29 ± 0.02	0.24 ± 0.07	0.14 ± 0.01
S	0.23 ± 0.1	0.22 ± 0.05	0.79 ± 0.24	0.74 ± 0.19	0.34 ± 0.07	0.64 ± 0.14	0.03 ± 0.00
O*	22.57 ± 0.1	6.15 ± 2.83	9.52 ± 1.40	12.92 ± 0.98	9.87 ± 2.83	20.62 ± 2.93	8.66 ± 1.10
O/C ratio	0.70 ± 0.10	0.38 ± 0.04	1.02 ± 0.16	1.24 ± 0.12	0.68 ± 0.15	2.30 ± 0.07	1.78 ± 0.08
H/C ratio	0.12 ± 0.01	0.13 ± 0.01	0.21 ± 0.01	0.22 ± 0.01	0.15 ± 0.01	0.20 ± 0.01	0.30 ± 0.01
HHV_{HC} (MJ kg^{-1})	12.81	5.80	2.98	3.45	5.06	1.71	0.76
HHV_{gas} (MJ kg^{-1})	NA	0.04	0.22	0.64	0.36	0.28	0.55
Carbon recovery (%)	NA	26.37	17.03	18.34	28.74	16.26	10.04
Energy recovery (%)	NA	24.10	13.77	15.41	25.45	7.87	3.96
Surface area and porosity measurement							
S_{BET} (m^2 g^{-1})	NA	3.970	12.20	12.17	23.21	8.650	10.45
D_P (nm)	NA	14.78	16.14	13.42	15.09	19.88	16.28
Pore vol. (cm^3 g^{-1})	NA	0.015	0.049	0.041	0.088	0.043	0.043

[a] S_{BET}; specific surface area D_P; average pore width, pore vol.; total pore volume, O*; calculated as a difference between 100-sum(CHNS + ash).

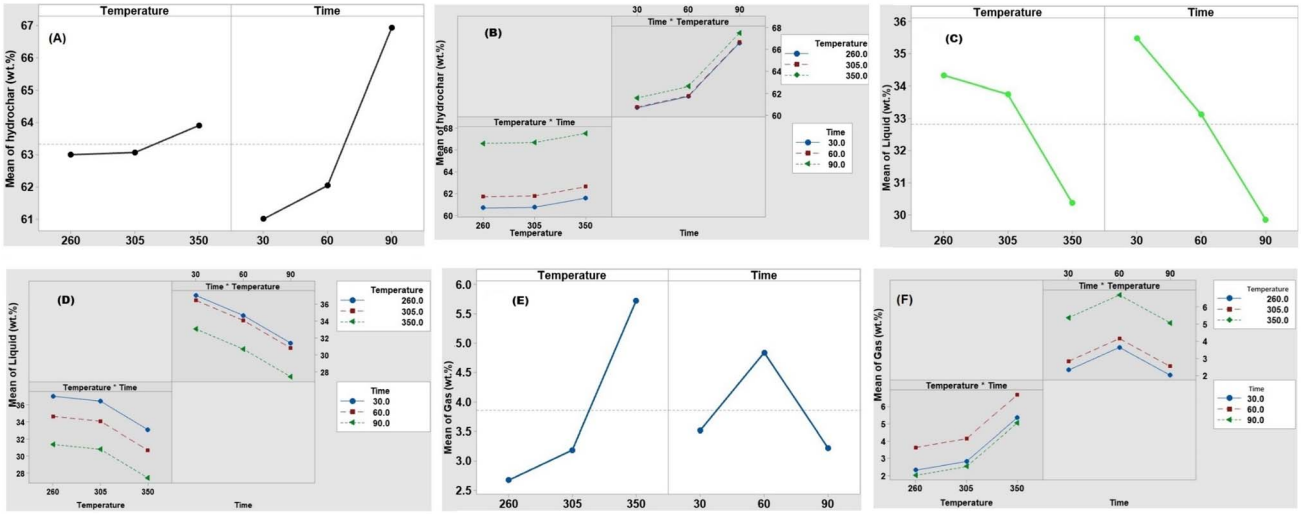

Fig. 2 Factorial plots showing the interaction effects of temperature and residence time on product yields. Plots (A) and (B) illustrate the effects and interactions for hydrochar yield, (C) and (D) for liquid products, and (E) and (F) for gaseous products, respectively.

was largely attributed to *in situ* synergistic contribution from different plastic types, cellulose and transitional metal inorganics within the heterogeneous feedstock that reduced the higher thermal degradation temperatures often required for the individual polymers.[57] Results in Table 2 show the statistical fit of the parameters and the products. The p value < 0.05 signifies that both temperature and time were relevant for the hydrothermal valorization with the coefficient of determination (R^2) >0.99. The higher F statistics values signifies the more significant effect on the product yield.[58] Therefore, time had a higher effect on hydrochar and liquid formation, while temperature was critical to the formation of gas products. Based on the highest hydrochar yield obtained at 350 °C and 90 minuets, and the complex polymeric nature of the feedstocks, further parameter optimizations such as catalyst loading, feedstock concentration and different catalysts were performed to elucidate on the effect of product yields and their physicochemical properties.

3.2.2 Ionization and thermodynamic properties water products. The ionization constant (K_w) and density (ρ) of water are among the major thermodynamic drivers that makes water a fluid above its critical point, thus, enabling it to solubilize and precipitate organics and inorganic compounds. During the non-isothermal heating ramping below 350 °C as shown in Fig. 3(A), K_w increased significantly by 278 times from 18 to 351 °C owing to higher dissociation of hydrogen bonds of water to ions at increasing temperature. In addition, the average enthalpy change (ΔH) during non-isothermal reaction was 36 kJ mol^{-1}, an endothermic process that takes in heat and shifts the equilibrium towards more dissociation. As a result of the autogenous pressure generated due to the increasing temperature to break down the feedstock, the water became compressed and hence, ρ decreased.

However, transitioning from non-isothermal to isothermal reaction duration, the ionization product of water reduced which was attributed to the effect of dielectric constant that becomes low at high temperature, thus lowering ionization potential of water. As shown in Fig. 3(B), at near-critical water a slight change in pressure increased K_w proportionally with density because greater molecular proximity enhances hydrogen bonding networks and ionic stabilization. Table 3 shows the average thermodynamic property changes during the 90 minutes isothermal reaction at three different reaction temperatures. At about 260 °C, the density and ionic products

Table 2 Factorial model analysis of variance for the solid, liquid and gas products produced at 30, 60, 90 minutes and 260, 305, 350 °C

	Hydrochar			Liquid			Gas		
	Temperature	Time	Model	Temperature	Time	Model	Temperature	Time	Model
Sum of squares	0.240970	0.234927	0.240970	0.213222	0.369776	0.582997	0.98773	0.29949	1.28723
Mean squares	0.060242	0.117464	0.060242	0.106611	0.369776	0.145749	0.493867	0.149746	0.321806
Degrees of freedom	2	2	4	2	2	4	2	2	4
F-Value	99576.62	194159.50	99576.66	1511.75	2621.73	2066.74	293.73	89.06	191.39
P-Value	0.0001	0.0001	0.000	0.0001	0.0001	0.000	0.0001	0.0001	0.000
Remark	—	Significant	—	—	Significant	—	—	Significant	—
Error	0.000002	0.000002	0.000002	0.000282	0.000282	0.000	0.000002	0.000002	0.000002
R^2	1.00	1.00	1.00	0.9995	0.9995	0.9995	0.9948	0.9948	0.9948
Adjusted R^2	0.9999	0.9999	0.9999	0.9990	0.9999	0.9999	0.9999	0.9999	0.9999

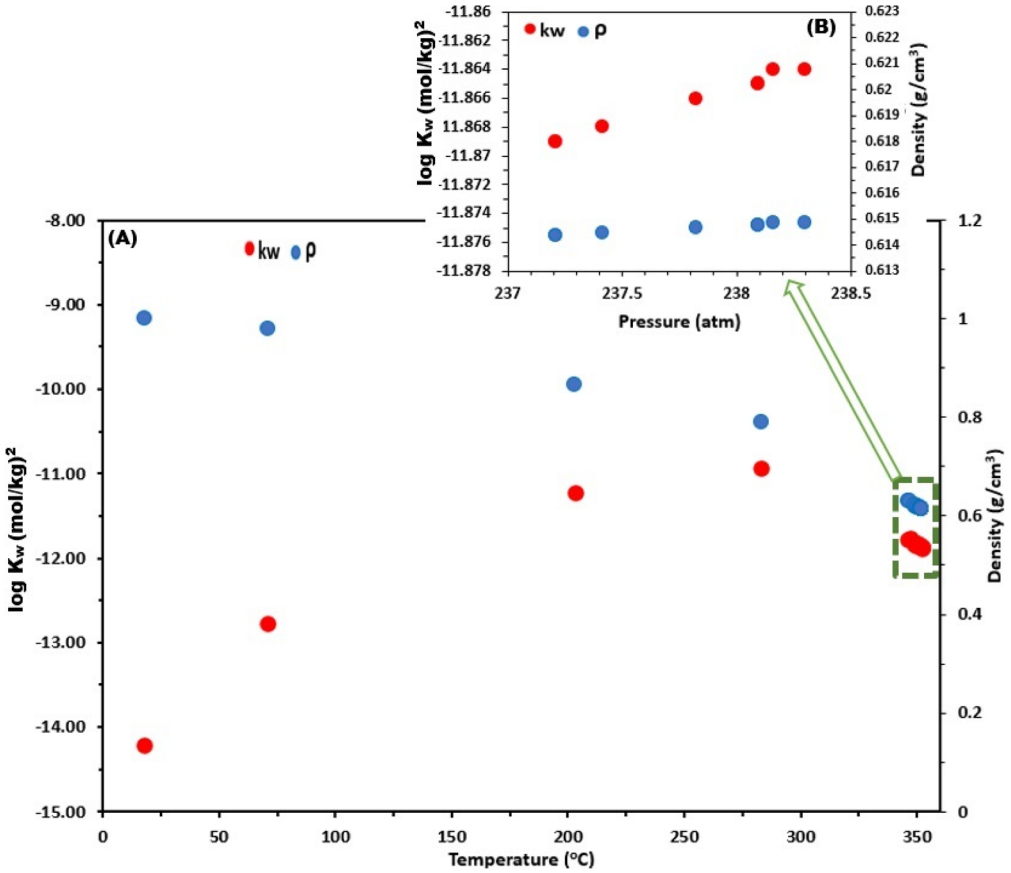

Fig. 3 (A) Variation of the ion product and density of water with temperature over a reaction duration of 150 minutes, and (B) variation of the ion product and density of water with pressure under isothermal conditions at 350 °C for a reaction duration of 90 minutes.

were moderate possibly due to hydrolysis reactions solubilizing more organics, resulting in low heat released (ΔH) and small ordering effect (ΔS).

The isothermal reactions at all investigated temperatures proceeded exothermically and the heat energy released increased sharply with increase in temperature. At elevated temperature (~305 °C), more exothermic and more ordering was observed, plausibly due to the radical cracking in the polymer structure becoming pronounced, thus, yielding more hydro char. At ~350 °C, very exothermic reaction and strong ordering effect were obtained. Hence yielding the highest hydrochar and gas products as observed in Fig. 2.

3.3. Parameter optimization

3.3.1 Effect of catalyst loading. Previous work involving comparison of nickel on silica–alumina (NiSiAl) and alkali-based catalysts, the former was performed on a fixed one feedstock-to-catalyst ratio to investigate the gas selectivity.[48] Thus, the effect of catalyst loading on different product yields was investigated as shown in Fig. 4. Significant increase in liquid yield was observed with a decrease in feedstock-to-catalyst ratio, with highest yield of 36% registered at the ratio of 1. The increase in Ni loading was selective in promoting the breakdown of complex polymers and organic component in ASR into more liquid products than solid and gas yields. In addition, at higher Ni loading, reaction conditions such as temperature and pressure were optimized to favor the formation of more liquid products. Moreover, nickel-based catalyst was reported to suppress tar formation because of enhanced ability to crack organic compounds.[59] Contrary to the liquid yield trend, the hydrochar and gas yields decreased with decreasing feedstock-to-catalyst ratio. This was attributed to the formation of carbonaceous deposits enhanced at low catalyst loading. As observed in the liquid reactions, increasing catalyst loading suppressed

Table 3 Averages of the thermodynamic properties of water during the 90 minutes isothermal reaction at temperature conditions of 260, 305 and 350 °C

T (°C)	P (atm)	ρ (g cm^{-3})	Log K_w (mol kg^{-1})^2	ΔG (kJ mol^{-1})	ΔH (kJ mol^{-1})	ΔS (kJ mol K)$^{-1}$
260.690 ± 1.75	130.988 ± 1.51	0.793 ± 0.00	−11.124 ± 0.00	113.680 ± 0.39	−5.914 ± 1.7	−0.224 ± 0.00
305.200 ± 0.84	173.503 ± 1.46	0.720 ± 0.00	−11.294 ± 0.01	125.043 ± 0.24	−45.019 ± 2.45	−0.294 ± 0.00
350.450 ± 1.71	234.578 ± 3.71	0.619 ± 0.00	−11.841 ± 0.03	141.356 ± 0.77	−142.876 ± 0.88	−0.456 ± 0.13

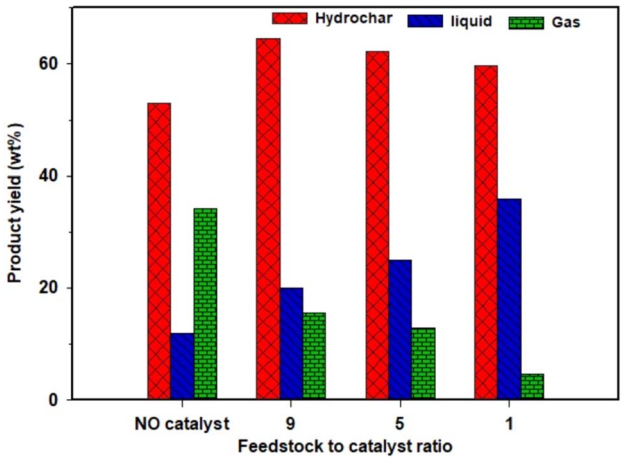

Fig. 4 Effect of ratio of feedstock to catalyst loading on product yield at 350 °C, average 21.1 MPa, 1.5 h, NiSiAl.

the polymerization and condensation reactions that typically lead to char formation, hence, low hydrochar at ratio of 1. Since Ni can enhance hydrogenation reactions, increasing its loading might have promoted hydrogenation and other reactions by converting gaseous products to liquid products, hence, reducing the overall gas yield. The non catalyzed reactions were solely driven by thermal decomposition. Thus, produced the lowest hydrochar and liquid yields, but had the highest overall gas yield attributed to solely CO_2 production.

3.3.2 Effect of feedstock concentration. The balance of ratio of water to feedstock is important variable for optimal valorization of biomass and complex heterogeneous mixed feedstocks.[60] As shown in Fig. 5, the hydrochar and liquid yields increased with increase in water-to-feedstock ratio. Water acts as a solvents that offers enhanced heat and mass transfer during hydrothermal processing, and reduces viscosity in liquid products, hence, leading to improved overall liquid yield.[61] In addition, rapid change in water physicochemical properties such as density offer significant changes in solvation power and molecular diffusivity leading to better quality liquid product

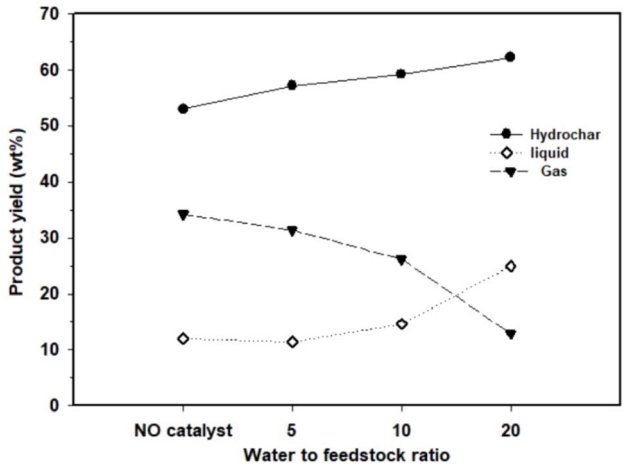

Fig. 5 Effect of feedstock concentration on product yield at 350 °C, average 21.1 MPa, 1.5 h, feedstock-to-catalyst ratio of 5.

than pyrolysis.[62,63] Increasing water-to-feedstock ratio increased the polymerization and decomposition of water-soluble products resulting in higher liquid and solid products.[64,65] 20 : 1 water-to-feedstock was the optimal ratio for ASR recycling at the investigated condition. Ong and team reported a range of 3 : 1 to 10 : 1water-to-waste ratio as the optimal ratios for hydrochar from hydrothermal co-processing LDPE and hyacinth.[66] Darzi *et al.*, reported an optimal 30 : 1 water-to-waste ratio during the hydrothermal valorization of polyethylene-terephthalate and nylon-6 mixture to yield 75% yield of the solid product.[67] Hydrothermal carbonization (HTC) of PVC and PS produced maximum hydrochar yield using water-to-waste ratio of 1 : 1 to 5 : 1 and 1 : 2 to 2 : 1, where these ratios enhanced dichlorination, reduced viscosity of liquids and effective heat transfer.[68–70] Literature reported varying water-to-feedstock ratios and this can be attributed to varying feedstock types. However, to balance between reduced energy needs, reduced reactivity and the reaction kinetics, plastics and mixed waste HTC were reported to be optimized in the range of 5 : 1 to 20 : 1 water-to-waste ratio.[71–74] The lowest liquid and solid products were obtained without catalyst, plausibly due to lower ionic strength of water that did not favor accelerated hydrolysis and depolymerization of plastic feedstock compared to when catalyst was used. Thus, without catalyst reactions kinetics was dictated by thermal water gas shift reaction, hence, more CO_2 gas yield.

3.3.3 Effect of catalyst type. The application of catalysts is important to achieve successful hydrothermal conversion of plastics to valuable products at reduced temperatures. Catalysts accelerate reaction rates and help in lowering activation energy at subcritical water conditions, thereby enhancing product selectivity and the thermal depolymerization of complex plastic polymers into useful monomers.[75] Fig. 6 shows the role of different catalysts towards gas selectivity and overall product yields. All catalysts showed a similar overall product yield trend in order of hydrochar > liquid > gas, while non catalyzed reactions followed a hydrochar > gas > liquid trend. This was attributed to catalysts ability to control reaction rates better than non catalyzed reactions. Ni-based catalysts enhanced the production of hydrochar and liquid products compared to Ru-based and non catalyzed reactions. Ni catalysts offer strong ability in cleavage of the C–C, O–H, C–H bonds, and promotes tar cracking, resulting in improved conversion efficiency and decomposition of recalcitrant long chain polymer derivatives to simple monomers.[76,77] NiSiAl catalyzed reaction promoted water-gas-shift and hydrogenation reactions that led to production of high hydrogen.[78] The below limit of detection for carbon monoxide and methane confirms that Ni-based catalyzed reactions did not proceed *via* steam reforming that was reported to require high temperatures[79] or methanation.[80] Ru/Al_2O_3 produced the lowest hydrochar and the highest CO_2 among catalyzed reactions. The low hydrochar was attributed to Ru/Al_2O_3 ability to limit char and tar formation.[81] Other studies reported Ni and Ru-based catalysts as robust catalysts for decomposition of organic materials by promoting water-gas-shift reaction to yield H_2, and Ni performed better than Ru catalysts.[82] Noteworthy, without catalyst, the gas product was

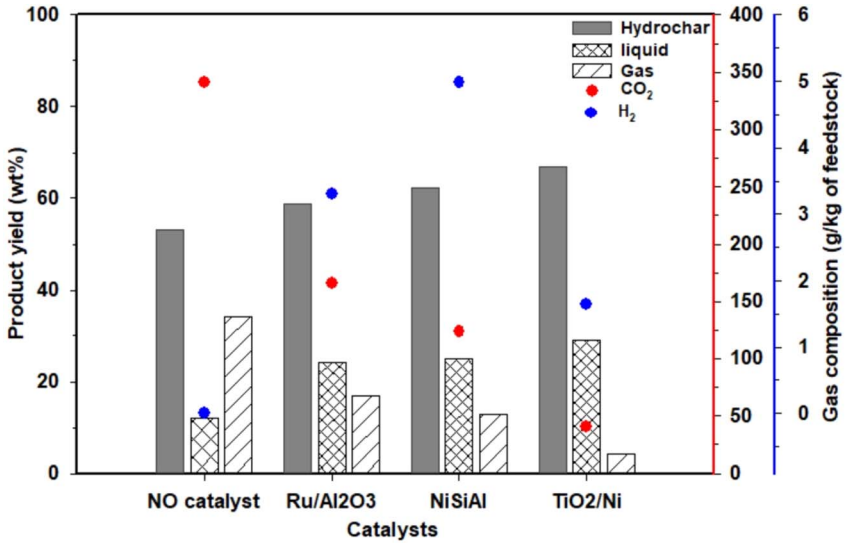

Fig. 6 Effect of catalyst on product yield at 350 °C, average 21.1 MPa, 1.5 h, catalyst to feedstock ratio of 5.

composed of only CO_2, and low hydrochar and liquid yields. This was attributed to water being the primary factor influencing the product composition, thereby the feedstock thermal decomposition to gas distribution was shifted to carbon dioxide.

3.4. Product characterization

3.4.1 Organic liquid analysis. The chemical composition of the organic oil phase was obtained using the GC-MS analysis as shown in Fig. 7. The oil products consisted of majorly organic compounds with carbon ranging from C6–C21, for instance, hydrocarbons, phenols, phenol-derivatives (*e.g.*, cresols and eugenols), amines (majorly aniline), ketones, and other organic compounds. The peak areas of major components with above 90% NIST match were the only chemical groupings considered in this study. The term others represent all other compounds <90% NIST match. As shown in Fig. 7(A), the product selectivity was dependent on the catalyst type deployed. For example, NiSiAl and Ni/TiO_2 catalysts promoted the production of relatively lower carbon phenolic derivatives (<C10) and nitro-aromatics. Ni sites promote hydrogen transfer and C–O bond cleavage, while alumina or titania supports provide acid sites that stabilize intermediates and enhance selectivity toward low-carbon phenolics (<C10). For example, the observed conversion of cresol to phenol at high water-to-solid ratios suggests a catalytic hydro-dealkylation mechanism involving surface-mediated C–C bond scission adjacent to the aromatic ring. While Ru/Al_2O_3 was selective for mainly ketones and <10% of phenolic compounds. The formation of ketones such as 4-phenylcyclohexanone, was attributed to Ru/Al_2O_3's redox cycling of intermediates like alcohols. Without catalyst, wide range of oil products with carbon between C6–C29 were obtained, containing a wide variety of chemical groupings. Thus, catalysis is needed to control reaction pathways for selective production of useful organics that can be upgraded with few additional post-treatment steps. NiSiAl catalyst showed the highest selectivity of useful phenolics (such as phenol, cresols, *etc.*) and aniline, therefore, was further investigated for feedstock concentration and catalyst loading effects. As shown in Fig. 7(B), the change in feedstock concentration from 5–10% maintained similar carbon distribution in the range of C6–C9. However, there were noticeable changes in the quantities of organic groupings and reaction pathways owing to changes in reaction conditions. At low feedstock concentration (5 wt%), oil products distribution comprised of majorly phenolics and amines (namely aniline). However, increasing the feedstock concentration to 10 and 20 wt%, reduced the amount of phenolics and amines while promoting the production of hydrocarbons and ketones, respectively. This can be attributed to the solubilization effect whereby when the feedstock concentration is high, the water-to-solid ratio drops, hence reducing the dilution of dissolved organics lead to enhanced deoxygenation of phenolics to hydrocarbons. In addition, the selectivity of ketones at high feedstock concentration can be attributed to a series of reactions such as oxidation followed by catalytic reduction to yield ketones such as 4-phenylcyclohexanone. In contrast to the former mechanistic pathways, for instance, the increase in feedstock concentration from 5 to 20 wt% resulted in the C6 compounds such as phenol area percent increasing from 11 to 23%, and the C7 compounds such as p-cresol area percent decreasing from 23 to 0%, respectively. The observed change in reaction pathway from C7 (methyl phenol) to C6 (phenol) compounds can be attributed to presence of high water-to-solid ratio that offer excellent solubilization and selectivity for catalytic dealkylation reaction[83] while suppressing coke formation.[84] Noteworthy, that the plausible pathway from methyl phenol to phenol was achieved in a single-reactor *in situ* conversion as opposed to literature reported series of operations such as feedstock fractionation to phenolic monomers followed by hydro-processing and then dealkylation to yield phenol in separate reactors.[83] Therefore, this study offers a cost-effective green alternative to production of high value-chemicals such

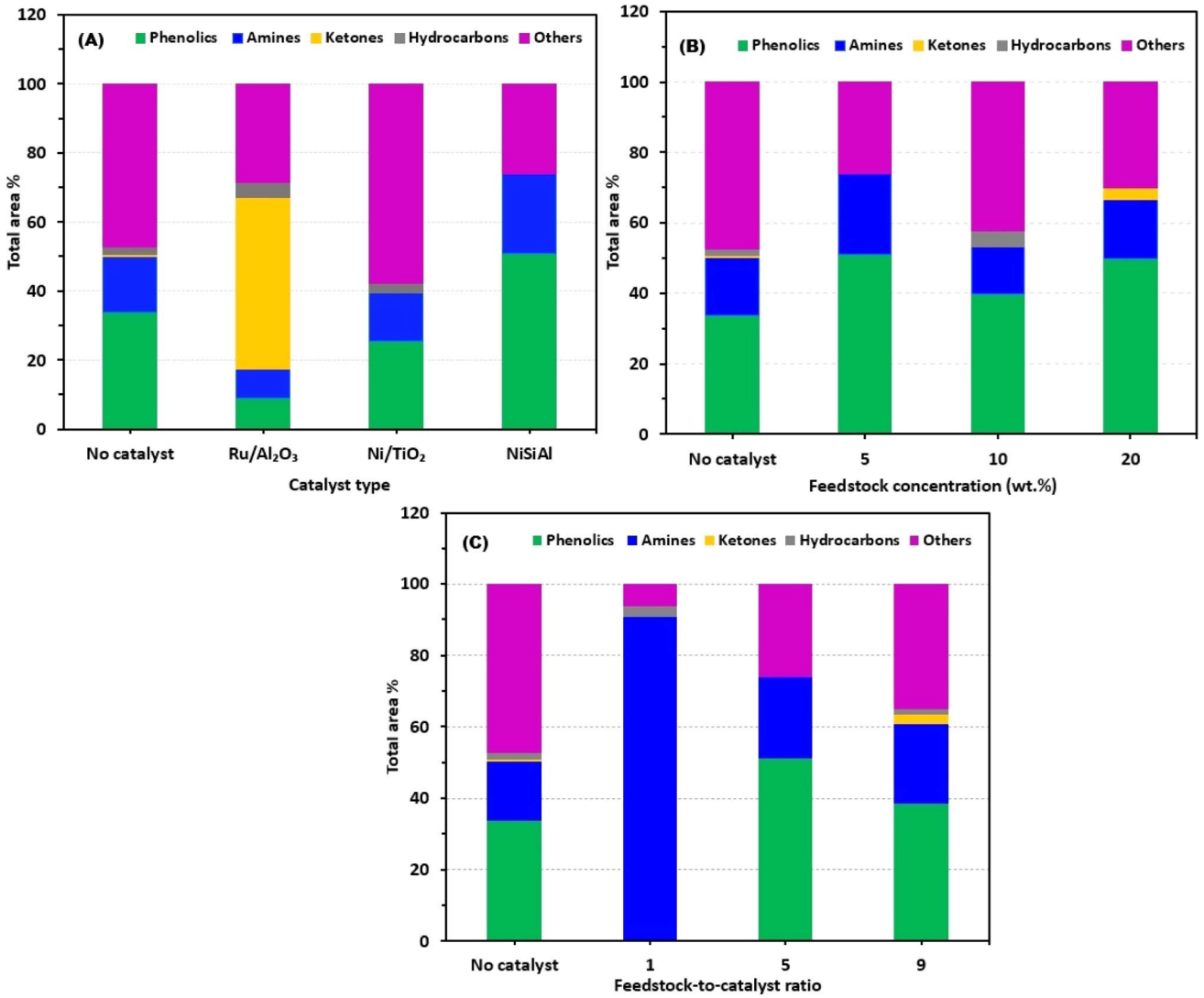

Fig. 7 Major chemical groupings in the organic oil phase for different experimental conditions obtained from GC-MS analysis for different reaction conditions of (A) catalyst type, (B) feedstock concentration and (C) feedstock-to-catalyst ratio.

as phenol that find wide industrial application in agrochemical, pharmaceutical, dyes, detergents and plastic sectors.[83]

Optimal feedstock-to-catalyst ratio is critical to product selectivity, therefore, altering the ratio of feedstock to catalyst had an effect on the oil product distribution, suggesting a change in reaction pathways (see Fig. 7(C)). For instance, equal ratio of feedstock-to-catalyst yielded a total area percent > 90% of C13 aromatic amines and 3% area percent of cyclododecane. Increasing the ratio to 5, drastically reduced the aromatic amines while enhancing majorly phenolic monomers in the carbon range of C6–C10. The drop in aromatic amines was plausibly due to reduced secondary reactions as catalyst amount was reduced, hence deamination reactions leading to dominant phenolic monomers from hydrothermal primary cracking. Further increment in the feedstock-to-catalyst ratio led to a wider products profile similar to observations without catalyst. This was attributed to low catalyst amount over the feedstock causing a reduction in the catalyst availability per reacting molecule. The fraction categorized as "Others" comprises a diverse range of compounds, including low-to high-molecular-weight phenolics (*e.g.*, phenol), carboxylic acid esters (*e.g.*, formic acid phenyl ester), cyclic ketones (*e.g.*, 2,3,4-trimethyl-2-cyclopenten-1-one), and heteroaromatic amines (*e.g.*, ethyl pyrazine). However, several compounds within this group did not meet the required National Institute of Standards and Technology (NIST) library quality match threshold of greater than 90%. Consequently, their identification remains tentative. Future work will involve more detailed characterization to confirm the composition and molecular structure of this fraction. Fig. 8 shows a summary of the different suggested mechanistic reaction pathways from ASR polymers to valuable oil products as identified in the GC-MS analysis.

3.4.2 Aqueous liquid analysis. Fig. 9 shows results of total organic carbon (TOC), total carbon (TC) and inorganic carbon (IC) distribution in the aqueous phase of the liquid product. Catalyzed reactions generated higher organic and inorganic

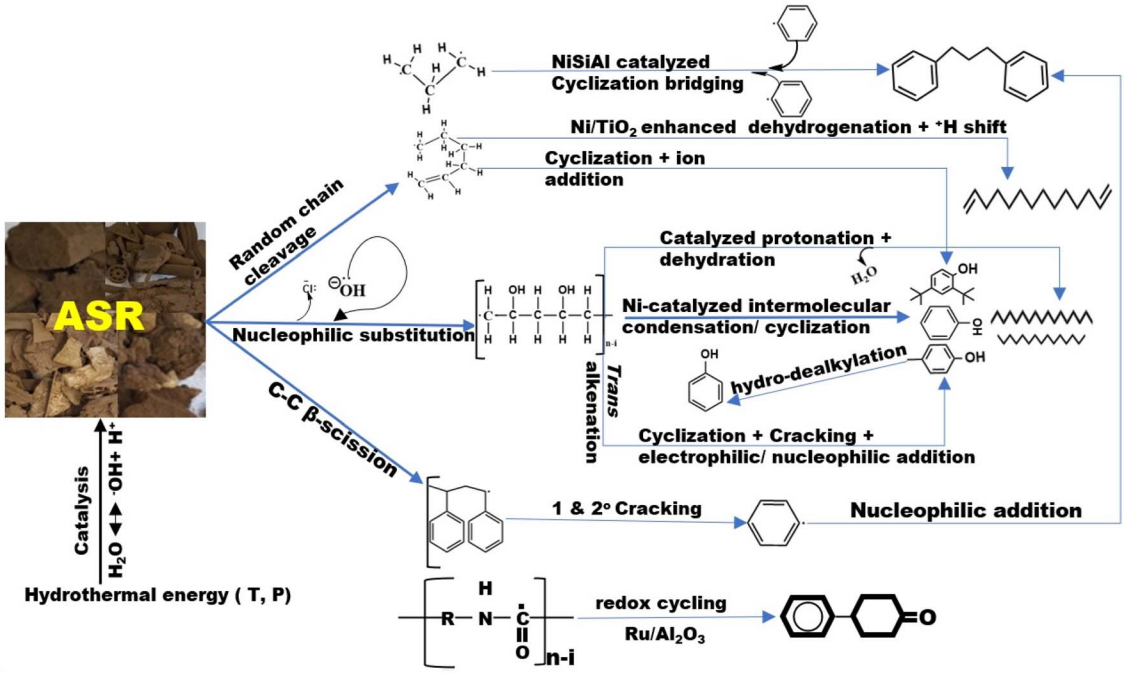

Fig. 8 Suggested reaction mechanisms and pathways of selected compounds identified in organic oil fraction.

carbon in the aqueous phase than non-catalyzed reactions. Catalytic hydrolysis enhanced breakdown of organic monomers that were likely soluble in aqueous phase, hence increased total carbon.[85] As shown Fig. 9(A), the increase in feedstock concentration decreased the amount of organic carbon in the aqueous products. This was attributed to the phase competition where solubilization for solids and organic oils was more favored than one in the aqueous phase as evidenced by the high hydrochar yields and GC-MS analysis product compositions. In addition, the increasing feedstock concentration can lead to the formation of complex or larger molecules that are less water-soluble, hence, less TOC. Application of different catalysts

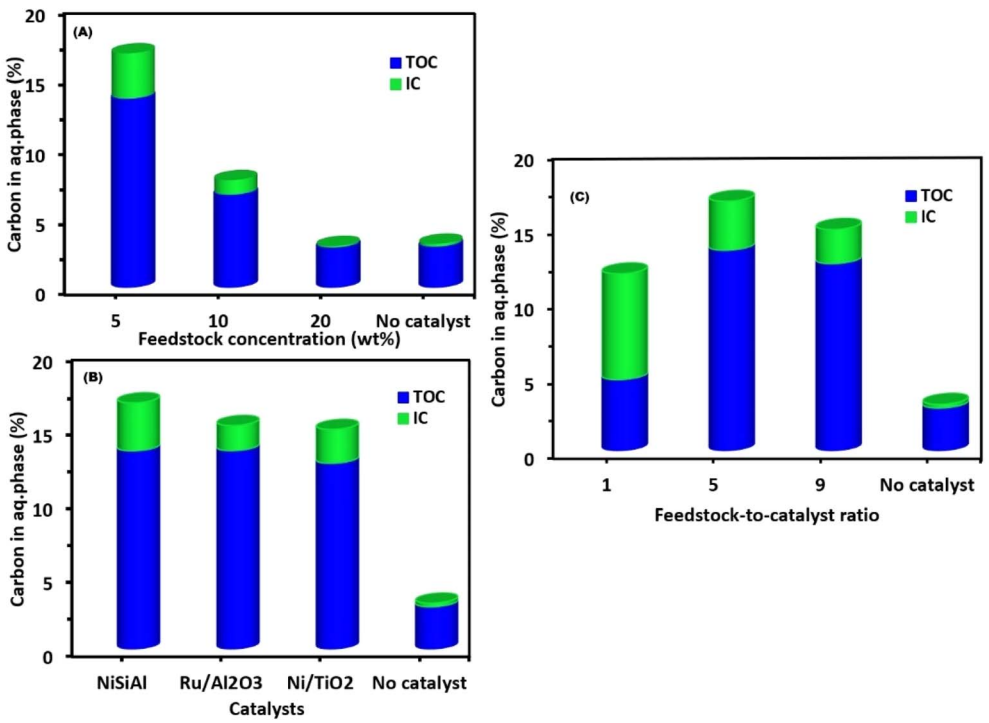

Fig. 9 Carbon distribution in aqueous phase investigated at different (A) feedstock concentrations (B) catalysts and (C) feedstock-to-catalyst ratio. Reaction conditions: 350 °C, 90 min, 5 wt% feedstock concentration for all catalysts, no catalyst and feedstock-to-catalyst ratio.

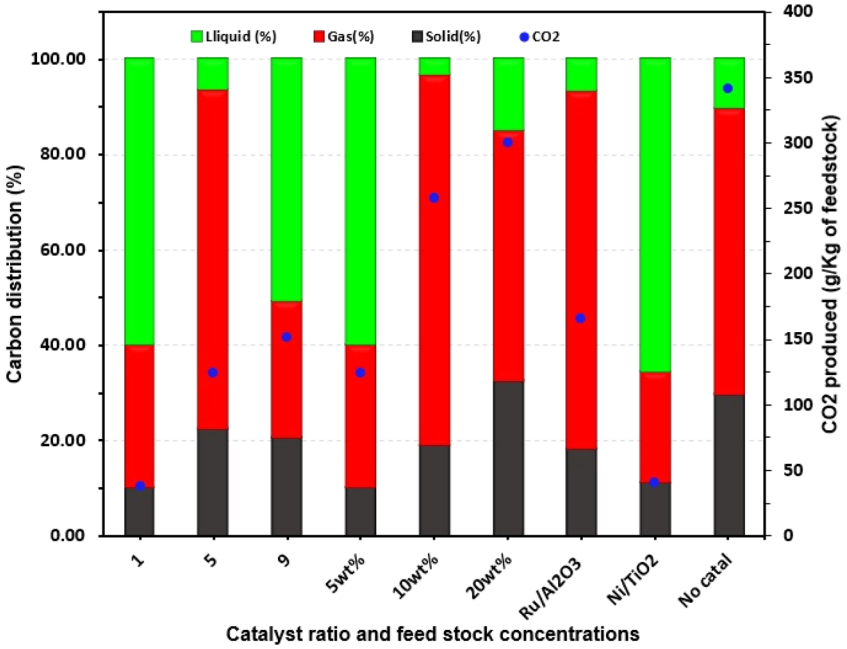

Fig. 10 Carbon balance for the feedstock-to-NiSiAl catalyst ratio of, 1–9 feedstock concentrations (5–20 wt%) and different catalysts. Reaction conditions: 350 °C, 90 min.

produced relatively equal carbon distribution in the aqueous phase (see Fig. 9(B)). For instance, NiSiAl had the highest 16.68% total carbon followed by 15.13% and 14.87% for Ru/Al_2O_3 and Ni/TiO_2, respectively. Noteworthy, nickel-based catalysts were more selective for inorganic carbon than ruthenium-based catalyst. Based on its highest total organic carbon, NiSiAl was further investigated on feedstock-to-catalyst ratio basis as shown in Fig. 9(C). Increase in feedstock-to-catalyst ratio from 1 : 1 to 5 : 1 increased the TOC by 1.4% from 11.84%. However, further increase to 9 : 1 ratio slightly reduced the TOC by 0.89%, signifying the role of optimal catalyst amount in solubilizing aqueous organic compounds.

3.4.3 Carbon balance. The carbon distribution in solid, liquid and gas products at different optimized conditions is shown in Fig. 10. As the feedstock-to-catalyst ratio increased from 1 : 1 to 5 : 1, there was a 41 and 12% carbon increase in the gas and solid phases, respectively, at the expense of a 53% carbon decrease in the liquid products. This was attributed to carbon transfer across the three products caused by changes in catalytic reaction pathways. Moreover, the many higher carbon organics (>C10) in the oil phase observed by GC-MS analysis at the 1 : 1 ratio were not detected at the feedstock-to-catalyst ratio 5 : 1. Therefore, the carbon distribution in the liquid product at feedstock-to-catalyst ratio 5 : 1 can be attributed mainly to the higher TOC and TC observed in the aqueous phase. When feedstock-to-catalyst ratio was further increased to 9 : 1, the >C10 compounds reappeared in the GC-MS results while lower TC in the aqueous phase was obtained, hence, a similar carbon transfer phenomenon plausibly happened.

Increasing feedstock concentration from 5 to 20 wt% increased carbon in the solid product by 3.17% owing to increase in elemental carbon as showed in Table 1. The high carbon distribution in the liquid products at 5 wt% was attributed to the wide range of organic carbon (C6–C13) in the oil phase and the highest 13.42% carbon in the aqueous phase. However, when feedstock concentration increased to 10 wt%, more carbon was distributed toward gas products owing to 2.08 times increase in the grams of CO_2 produced per kilogram of feedstock, and 2.05 times decrease of the carbon in the aqueous phase. Comparatively, NiSiAl with Ru/Al_2O_3 and Ni/TiO_2; Ru/Al_2O_3 catalysts showed similar carbon distribution as NiSiAl of feedstock-to-catalyst ratio 5 : 1 while Ni/TiO_2 catalyst products' carbon resembled NiSiAl of feedstock-to-catalyst ratio 5 : 1. Thus, a plausible similar catalytic reaction pathway, however, leading to different products as observed in the different oil

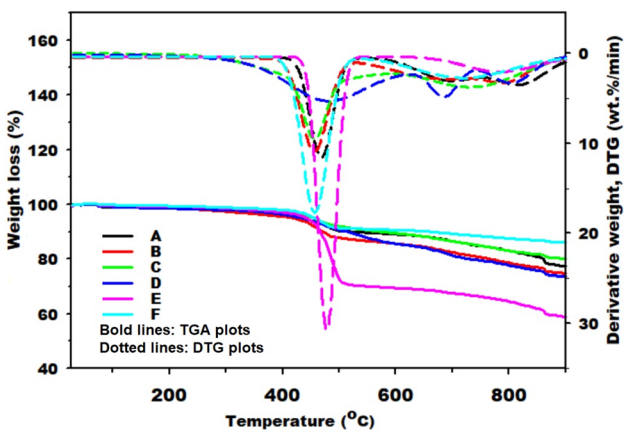

Fig. 11 TGA and corresponding DTG plots of hydrochar at conditions of (A) no catalyst, (B–D) feedstock concentrations (20–5 wt%) with NiSiAl catalyst ratio of 5, (E) Ru/Al_2O_3 and (F) Ni/TiO_2 catalysts, reaction conditions: 350 °C, 90 minutes.

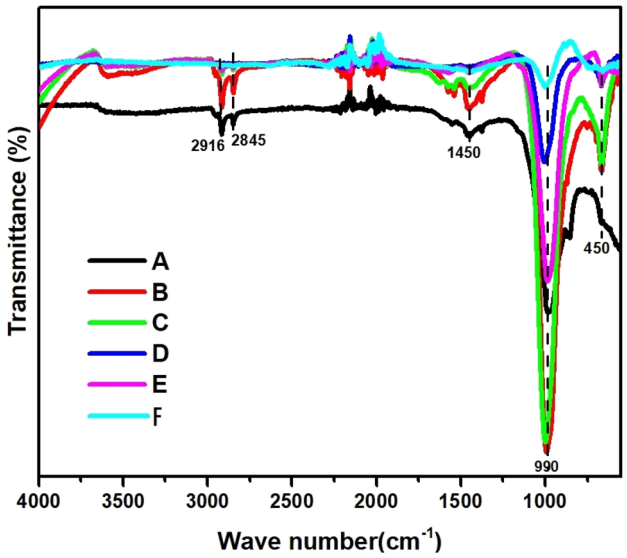

Fig. 12 Hydrochar FTIR plots obtained at conditions of (A) no catalyst, (B–D) feedstock concentrations (20–5 wt%) with NiSiAl catalyst ratio of 5, (E) Ru/Al_2O_3 and (F) Ni/TiO_2 catalysts, respectively.

phase products. The carbon distribution without catalyst was highest in the gas products due to the highest levels of CO_2 produced, 341.28 g Kg^{-1} of feedstock, as the only gas component. Furthermore, due to the low carbon in the aqueous product, and the many organic compounds in the oil phase (C6–C29), the carbon distribution in the liquid product of without catalyst was largely attributed to the carbon transfer in the organic oil phase. In addition, carbon in the solid product without catalyst was mainly as a result of elemental carbon transfer as evidenced in high elemental analysis of Table 1. Noteworthy, in all optimized runs, the carbon transfer in the gas products was majorly towards CO_2, it was the only detected carbon-containing product in the gas phase.

3.4.4 Hydrochar analysis. The TG/DTG curves of hydrochar at selected optimized conditions are presented in Fig. 11. Hydrochar at all investigated conditions showed enhanced thermal stability compared to the on-set degradation temperature of 425 °C, 200 °C higher than in original feedstock.[48] The enhanced stability was attributed to the concentration of inorganic elements as observed in the increased ash content in Table 1. NiSiAl catalyst with feedstock concentration >5% gave similar thermal degradation profile to non-catalyzed hydrochar with mass loss between 9–12%, thus, suggesting similarity in their thermal degradation kinetics. Ni/TiO_2 catalyzed hydrochar produced the highest mass loss of 31% at 476 °C, attributed to the volatile components. Moreover, this mass loss was consistent with the proximate volatile matter result (30.51%) reported in Table 1. Noteworthy, the maximum mass loss occurred in the temperature regime between 425–525 °C, signifying similarity in the thermal properties of the decomposing species within that temperature region.

Fig. 12 shows FT-IR spectra of the hydrochar at selected optimized conditions. All hydrochar at lower wave length <1500 cm^{-1} exhibited similar functional groups with different vibrational strength. The major absorption spectra between 1500 and 950 cm^{-1} was assigned to C–O stretching vibration attributed to the oxygen-containing functional groups such as alcohols, esters, as a result of depolymerization reactions, and the glycosidic bond often associated cellulosic material.[86] No wonder, the feedstock comprised of visible cellulosic materials as commonly used in the automotive cushions. Processing parameters such as feedstock concentration dictate hydrochar surface properties. For instance, at elevated feedstock concentration (10 and 20%), there were enhanced C–O owing to vibration of oxygen-containing compounds like phenols. In addition, the C–H stretching vibrations in the regime of 2916–2845 cm^{-1} was attributed to the symmetric and asymmetric aliphatic methylene groups of the aliphatic and aromatic

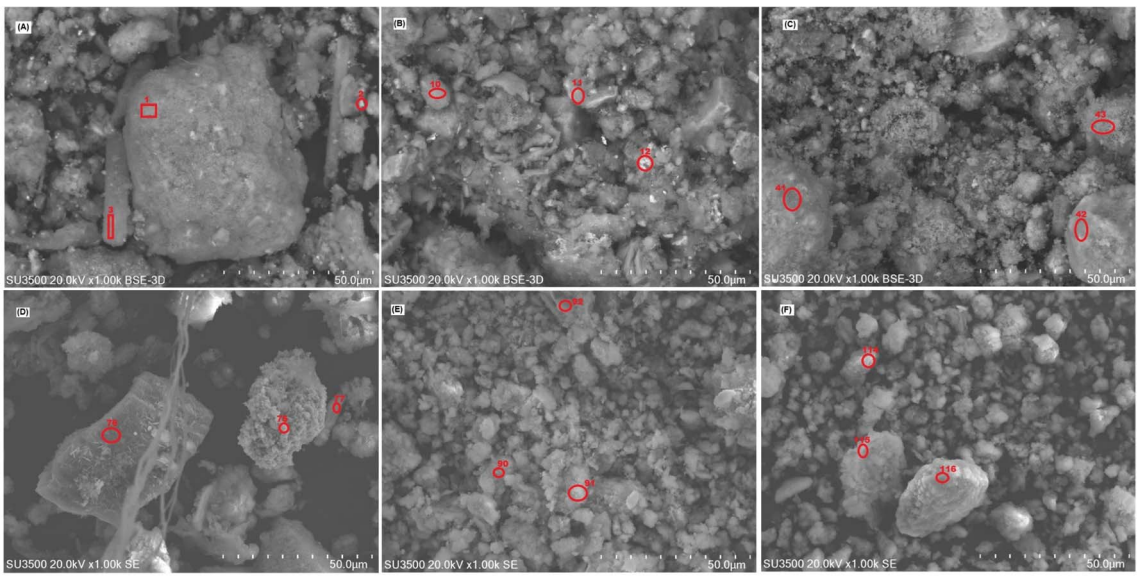

Fig. 13 SEM-EDX images and spectrum mappings of hydrochar produced at conditions of (A) no catalyst, (B–D) feedstock concentrations (20–5 wt%) with NiSiAl catalyst ratio of 5, (E) Ru/Al_2O_3 and (F) Ni/TiO_2 catalysts, respectively.

Table 4 EDX elemental composition of selected spectrum labels of hydrochar produced at reaction conditions of 350 °C, 150 minutes, feedstock-to-catalyst ratio of 5 and 5 wt% feedstock concentrations (for Ru/Al_2O_3 and Ni/TiO_2 catalyzed reaction)

	Feedstock concentrations (wt%) (catalyst; NiSiAl)																	
	No catalyst			20			10			5			Ru/Al_2O_3			Ni/TiO_2		
	Spectrum			Spectrum			Spectrum			Spectrum			Spectrum			Spectrum		
Elements	1 (wt%)	2 (wt%)	3 (wt%)	10 (wt%)	11 (wt%)	12 (wt%)	41 (wt%)	42 (wt%)	43 (wt%)	75 (wt%)	76 (wt%)	77 (wt%)	90 (wt%)	91 (wt%)	92 (wt%)	114 (wt%)	115 (wt%)	116 (wt%)
C	20.0	32.1	40.0	39.4	22.7	0.0	6.6	3.4	9.3	10.2	8.3	30.5	15.7	13.9	18.5	0	23.0	12.9
O	30.1	38.5	35.0	43.6	49.0	51.3	45.1	27.7	27.6	23.2	28.7	42.9	33.6	42.0	45.8	22.1	41.3	40.1
Si	12.8	6.0	5.5	4.6	6.2	15.7	3.2	2.0	3.0	1.0	10.3	7.3	5.5	2.5	7.6	12.3	7.0	3.5
Fe	17.4	18.2	10.1	5.0	12.0	15.8	2.6	3.6	11.3	56.2	44.8	6.5	3.6	32.4	10.3	8.8	7.0	33.3
Ni	0.0	0.0	0.0	0.0	0.0	0.0	4.7	5.7	4.7	0.0	0.0	0.0	32.6	5.54	7.3	47.3	13.9	4.0
Ca	8.2	1.3	2.4	1.4	1.8	1.0	0.62	1.2	1.5	2.6	4.8	0.8	3.1	2.3	0.6	0.9	0.7	0.8
Al	3.9	2.5	3.2	1.6	4.2	6.5	1.37	1.2	1.6	0.0	1.5	5.3	4.7	1.7	6.7	5.5	4.3	1.8
Na	0.6	0.0	0.0	0.0	0.0	0.0	0.0	0.0	0.0	0.0	0.0	0.0	1.3	0.0	0.0	0.0	0.0	0.0
K	1.6	0.7	0.3	0.0	0.0	0.4	0.0	0.0	0.0	0.0	0.0	0.0	0.0	0.0	0.0	0.0	0.0	0.0
Ti	0	0	0	0.0	0.0	0.0	30.7	40.1	27.6	0.0	0.0	0.5	0.0	0.0	0.0	0.0	0.0	0.0
Ba	0	0	0	0.0	0.0	0.0	0.0	15.0	13.5	3.9	0.0	0.0	0.0	0.0	0.0	0.0	0.0	0.0
Others	5.4	0.7	3.5	4.4	4.1	9.3	5.1	0.1	0.0	2.9	1.6	6.2	0.0	0.0	3.2	3.1	2.8	3.6

compounds, whose increased intensity signifies saturation of such compounds during hydrochar formation.[87] The presence of weak hydroxyl O–H vibration around 3500 cm^{-1} depicts dehydration during hydrochar formation, hence, increased thermal stability as observed in the TGA results.[88,89]

The results of surface morphologies of the selected hydrochar produced at different conditions is presented in Fig. 13. Without catalyst (Fig. 13(A)), the hydrochar produced regular packed carbonaceous chunks and cylindrical morphologies. The EDX spectral mapping in Table 4 revealed higher amount of carbon and iron, silica and aluminum oxides. The high carbon retention in the hydrochar as already revealed in the carbon balance can be attributed to the complex heterogeneous nature of the feedstock that without catalyst application, there is limited carbon conversion. Fig. 13(B–D) showed that varying the feedstock concentration altered the surface chemistries of hydrochar due to variance in reaction pathways such as polymerization and the degree of hydrolysis. For instance, at high feedstock concentrations (Fig. 13(B and C)) aggregates of fused and irregular morphologies were observed, owing to the limited amount of water resulting in incomplete hydrolysis causing partial degradation that yielded irregular block solids. However, at low concentration (5 wt%), regular morphologies were observed, plausibly due to the increased water amount that promoted complete hydrolysis and solubilization of organics leaving dispersed regular-shaped carbonaceous particles. The change in catalyst types such as Ru/Al_2O_3 and Ni/TiO_2 (Fig. 13(E and F)) yielded hydrochar of different sized-irregular morphologies, owing to difference in reaction mechanisms promoted by respective catalysts. Additional analyses on hydrochar using such as XRD and Raman spectroscopy, to elucidate on the degree of carbon ordering and better understand the structural evolution for a specific advanced application will be considered. Albeit limited equipment access, this study's assessment of thermal stability, surface functional groups, and morphological features, elucidate on the multi-purpose potential application of ASR hydrochar such as cement additive, hydrothermal metallurgical resource recovery, adsorbent, or as a fuel.

4. Conclusion

This study demonstrated the feasibility and optimization of catalytic hydrothermal conversion of heterogeneous end-of-life automotive fluff (AF) waste in near-supercritical water for the sustainable production of low-carbon fuels and high-value products. Temperature, reaction time, feedstock concentration, catalyst type, and catalyst loading were identified as key factors influencing product yields and selectivity across solid (hydrochar), liquid, and gaseous phases. The optimal conditions of 350 °C, 90 min, NiSiAl catalyst, 5–10 wt% feedstock concentration, and catalyst-to-feedstock ratio of 5 : 1 enhanced hydrochar stability, increased calorific value, and promoted selective production of phenolics and aromatic amines in the liquid phase, while minimizing undesirable gas-phase carbon losses.

The application of Ni-based catalysis proved essential for controlling reaction pathways, improving depolymerization efficiency, and suppressing tar formation, thereby enabling higher conversion of complex polymers into targeted monomers. NiSiAl exhibited superior performance in enhancing aqueous-phase organic carbon and phenolic selectivity, offering significant potential for direct feedstock-to products during industrial chemical production. In contrast, Ru-based catalysts favored ketone formation, while non-catalyzed reactions produced broader and less controlled product distributions dominated by CO_2.

Hydrochar characterization revealed improved thermal stability and distinct morphological changes influenced by feedstock concentration and catalyst choice. High ash content and stable functional groups indicate potential for applications in materials engineering or as solid fuels. Carbon balance analysis confirmed that catalyst type and loading dictate carbon

partitioning among product phases, with NiSiAl enabling efficient carbon transfer to valuable liquid and solid fractions.

Overall, catalytic hydrothermal processing in near-supercritical water offers a viable circular economy pathway for valorizing hazardous, energy-rich automotive shredder residue. By optimizing operational parameters and catalyst systems, this process can simultaneously address plastic waste challenges, reduce landfill burdens, and produce market-ready fuels and chemicals. Future work will address catalyst evaluation, explore continuous-scale integration with CCUS and targeted upgrading of phenolic-rich liquid products to maximize economic and environmental benefits.

Author contributions

Emmanuel Galiwango: conceptualization, methodology, formal analysis, writing – original draft, data curation, visualization, writing – review & editing. James Butler: supervision, funding acquisition, project administration, data curation, resources, review & editing. Samira Lotfi: investigation; funding acquisition, project administration, review & editing methodology, formal analysis, data curation. Weiguo Ma and Kevin Austin: visualization and methodology.

Conflicts of interest

The authors declare that there are not any known competing interests.

Data availability

All data supporting the findings of this study are included within the manuscript.

Acknowledgements

The authors would like to acknowledge financial support from OERD, Government of Canada grant number: A1-022498.

References

1 S. A. Pradeep, A. M. Deshpande, M. Limaye, R. K. Iyer, H. Kazan and G. Li, *et al.*, A Perspective on the Evolution of Plastics and Composites in the Automotive Industry, *Applied Plastics Engineering Handbook*, 2024, pp. 705–748.
2 W. Zhang and J. Xu, Advanced lightweight materials for Automobiles: A review, *Mater. Des.*, 2022, **221**, 110994.
3 H. Abedsoltan, Applications of plastics in the automotive industry: Current trends and future perspectives, *Polym. Eng. Sci.*, 2024, **64**(3), 929–950.
4 P. Kuiper and S. van Berkum, End-of-life vehicles, *Handbook of Recycling*, Elsevier, 2024, pp. 181–201.
5 J. R. Duflou, J. De Moor, I. Verpoest and W. Dewulf, Environmental impact analysis of composite use in car manufacturing, *CIRP Ann.*, 2009, **58**(1), 9–12.
6 M. Ravina, I. Bianco, B. Ruffino, M. Minardi, D. Panepinto and M. Zanetti, Hard-to-recycle plastics in the automotive sector: Economic, environmental and technical analyses of possible actions, *J. Cleaner Prod.*, 2023, **394**, 136227.
7 B. Ruffino and M. Zanetti, Is the assimilation to a solid recovered fuel a viable solution for automobile shredder residues' management?, *Environ. Res.*, 2024, **247**, 118131.
8 A. Kerric, M. J. Mazerolle, M. Sorais, J.-F. Giroux and J. Verreault, Impact of landfill characteristics on the atmospheric exposure to halogenated flame retardants in gulls, *Chemosphere*, 2023, **343**, 140207.
9 P. Stogiannis, A. Triantafillidis, P. Amarantos, I. Kontodimos, C. Ketikidis and P. Grammelis, Measuring the Concentration of Mercury for Automotive Shredded Residues Using the Direct Mercury Analyser, *Eng. Proc.*, 2023, **56**(1), 253.
10 P. Bentley, K. Williams and A. Khodier, How the physio-chemical properties of char from the pyrolysis of Automotive Shredder Residue (ASR) influences its future uses, *Pure Appl. Chem.*, 2023, **95**(5), 487–500.
11 C. Zambrano, A. I. Fernández, P. Tamarit and C. Barreneche, Mechanical-physical methods for paint removal of recycled bumpers for revalorization in the automotive industry, *Polym. Test.*, 2024, 108630.
12 V. K. Soo, J. Peeters, P. Compston, M. Doolan and J. R. Duflou, Comparative study of end-of-life vehicle recycling in Australia and Belgium, *Proced. CIRP*, 2017, **61**, 269–274.
13 J. Singh and B.-K. Lee, Pollution control and metal resource recovery for low grade automobile shredder residue: A mechanism, bioavailability and risk assessment, *Waste Manage.*, 2015, **38**, 271–283.
14 R. Cossu and T. Lai, Automotive shredder residue (ASR) management: An overview, *Waste Manage.*, 2015, **45**, 143–151.
15 A. Khodier, K. Williams and N. Dallison, Challenges around automotive shredder residue production and disposal, *Waste Manage.*, 2018, **73**, 566–573.
16 P. Evangelopoulos, N. Sophonrat, H. Jilvero and W. Yang, Investigation on the low-temperature pyrolysis of automotive shredder residue (ASR) for energy recovery and metal recycling, *Waste Manage.*, 2018, **76**, 507–515.
17 S.-J. Cho, H.-Y. Jung, Y.-C. Seo and W.-H. Kim, Studies on gasification and melting characteristics of automobile shredder residue, *Environ. Eng. Sci.*, 2010, **27**(7), 577–586.
18 J. Tan, W. Li, L. Tang, X. Chen, H. Liu and F. Wang, Study on the pyrolysis characteristics and char gasification kinetics of pre-separated automobile shredder residues, *J. Environ. Chem. Eng.*, 2024, **12**(2), 112520.
19 J. Maric, T. Berdugo Vilches, H. Thunman, M. Gyllenhammar and M. Seemann, Valorization of automobile shredder residue using indirect gasification, *Energy Fuels*, 2018, **32**(12), 12795–12804.
20 S.-Y. Cheng, N. T. N. L. Thao and K.-Y. Chiang, Hydrogen gas yield and trace pollutant emission evaluation in automotive shredder residue (ASR) gasification using prepared oyster shell catalyst, *Int. J. Hydrogen Energy*, 2020, **45**(42), 22232–22245.

21 S. A. Roh, W. H. Kim, J. H. Yun, T. J. Min, Y. H. Kwak and Y. C. Seo, Pyrolysis and gasification-melting of automobile shredder residue, *J. Air Waste Manage. Assoc.*, 2013, **63**(10), 1137–1147.

22 Q. He, W. Deng, K. Xu, L. Jiang, J. Xu, S. Su, *et al.*, Enhancing pyrolysis of automobile shredder residue through torrefaction: Impact on heavy components formation in oil, *Fuel Process. Technol.*, 2023, **252**, 107964.

23 Y. Ren, H. Hu, C. Cao, G. Guo, X. Zeng, C. Zou, *et al.*, Evolution and speciation transformation of chlorine during automobile shredder residue pyrolysis, *Waste Manage.*, 2024, **174**, 320–327.

24 M. K. Harder and O. T. Forton, A critical review of developments in the pyrolysis of automotive shredder residue, *J. Anal. Appl. Pyrolysis*, 2007, **79**(1–2), 387–394.

25 B. Boughton, Evaluation of shredder residue as cement manufacturing feedstock, *Resour. Conserv. Recycl.*, 2007, **51**(3), 621–642.

26 J. Lohse, K. Sander, M. Wirts, *Heavy Metals in Vehicles II - final repor*, Report compiled for the Directorate General Environment, Nuclear Safety and Civil Protection of the Commission of the European Communities by Ökopol - Institut für Ökologie und Politik GmbH, 2001, http://europa.eu.int/comm/environment/waste/studies/elv/heavy_metals.pdf.

27 Q. Liu, H. Zheng, P. Zhang, X. Guo, W. Deng, K. Xu, *et al.*, Enhancing pyrolysis of automobile shredder residue through torrefaction: Interactions among typical components, *Fuel*, 2025, **390**, 134670.

28 H. Bockhorn, J. Hentschel, A. Hornung and U. Hornung, Environmental engineering: stepwise pyrolysis of plastic waste, *Chem. Eng. Sci.*, 1999, **54**(15–16), 3043–3051.

29 P. Bentley, K. S. Williams and A. Khodier, *Improving Char and Oil for Commercial Applications from the Pyrolysis of Automotive Shredder Residue through the Use of Different Types of Catalysts*, WIT Transactions on Ecology and the Environment, 2023, pp. 139–149.

30 O. K. Choi, E. H. Song and H. Kim, Hydrothermal dechlorination strategy for high-quality oil recovery from polyvinyl chloride, *Sci. Total Environ.*, 2024, **947**, 174599.

31 F.-R. Xiu, R. Yang, Y. Qi, K. Zhou, J. Wang, W. Shao, *et al.*, High-efficiency promotion on dechlorination of polyvinyl chloride in subcritical water treatment by introducing waste concrete, *Process Saf. Environ. Prot.*, 2023, **174**, 1056–1064.

32 P. Zhao, Z. Li, T. Li, W. Yan and S. Ge, The study of nickel effect on the hydrothermal dechlorination of PVC, *J. Cleaner Prod.*, 2017, **152**, 38–46.

33 J. Li, B. R. Pinkard, S. Wang and I. V. Novosselov, Hydrothermal treatment of per-and polyfluoroalkyl substances (PFAS), *Chemosphere*, 2022, **307**, 135888.

34 K. Sue, A. Suzuki, M. Suzuki, K. Arai, Y. Hakuta, H. Hayashi, *et al.*, One-pot synthesis of nickel particles in supercritical water, *Ind. Eng. Chem. Res.*, 2006, **45**(2), 623–626.

35 B. R. Foy, K. Waldthausen, M. A. Sedillo and S. J. Buelow, Hydrothermal processing of chlorinated hydrocarbons in a titanium reactor, *Environ. Sci. Technol.*, 1996, **30**(9), 2790–2799.

36 M. J. Boel, H. Wang, A. A. Farra, L. Megido, J. M. González-LaFuente and N. R. Shiju, Hydrothermal liquefaction of plastics: a survey of the effect of reaction conditions on the reaction efficiency, *React. Chem. Eng.*, 2024, **9**(5), 1014–1031.

37 C. A. Che and P. M. Heynderickx, Hydrothermal carbonization of plastic waste: a review of its potential in alternative energy applications, *Fuel Commun.*, 2023, 100103.

38 M. K. Akalın, K. Tekin and S. Karagöz, Supercritical fluid extraction of biofuels from biomass, *Environ. Chem. Lett.*, 2017, **15**, 29–41.

39 H. D. D. Ziero, L. S. Buller, A. Mudhoo, L. C. Ampese, S. I. Mussatto and T. F. Carneiro, An overview of subcritical and supercritical water treatment of different biomasses for protein and amino acids production and recovery, *J. Environ. Chem. Eng.*, 2020, **8**(5), 104406.

40 G. R. Mong, H. Tan, D. D. C. V. Sheng, H. Y. Kek, B. B. Nyakuma, K. S. Woon, *et al.*, A review on plastic waste valorisation to advanced materials: Solutions and technologies to curb plastic waste pollution, *J. Cleaner Prod.*, 2023, 140180.

41 GRTgaz, Hydrothermal Gasification: the local recovery of a wide variety of waste rich in organic matter as renewable and low-carbon gas, *Hydrothermal Gasification: the Local Recovery of a Wide Variety of Waste Rich in Organic Matter as Renewable and Low-Carbon Gas*, 2024.

42 B. Zhang, B. K. Biswal, J. Zhang and R. Balasubramanian, Hydrothermal treatment of biomass feedstocks for sustainable production of chemicals, fuels, and materials: progress and perspectives, *Chem. Rev.*, 2023, **123**(11), 7193–7294.

43 Y. Wu, H. Wang, H. Li, X. Han, M. Zhang, Y. Sun, *et al.*, Applications of catalysts in thermochemical conversion of biomass (pyrolysis, hydrothermal liquefaction and gasification): A critical review, *Renewable Energy*, 2022, **196**, 462–481.

44 M. Wilk, A. Magdziarz, I. Kalemba-Rec and M. Szymańska-Chargot, Upgrading of green waste into carbon-rich solid biofuel by hydrothermal carbonization: The effect of process parameters on hydrochar derived from acacia, *Energy*, 2020, **202**, 117717.

45 H. Li, S. Wang, X. Yuan, Y. Xi, Z. Huang, M. Tan, *et al.*, The effects of temperature and color value on hydrochars' properties in hydrothermal carbonization, *Bioresour. Technol.*, 2018, **249**, 574–581.

46 J. González-Arias, M. E. Sánchez, J. Cara-Jiménez, F. M. Baena-Moreno and Z. Zhang, Hydrothermal carbonization of biomass and waste: A review, *Environ. Chem. Lett.*, 2022, 1–11.

47 S. K. Vijayan, V. Sahajwalla and S. Bhattacharya, Insights into the options of energy and metal recovery from automotive shredder residue: A review, *Resour. Conserv. Recycl. Adv.*, 2022, **15**, 200097.

48 E. Galiwango, M. Beaulne, J. Butler, W. Ma, K. Austin and S. Lotfi, Catalytic hydrothermal conversion of end-of-life

plastic waste in near supercritical water, *Int. J. Hydrogen Energy*, 2024, **87**, 1389–1403.
49 S. Channiwala and P. Parikh, A unified correlation for estimating HHV of solid, liquid and gaseous fuels, *Fuel*, 2002, **81**(8), 1051–1063.
50 E. Danso-Boateng, R. Holdich, S. Martin, G. Shama and A. D. Wheatley, Process energetics for the hydrothermal carbonisation of human faecal wastes, *Energy Convers. Manage.*, 2015, **105**, 1115–1124.
51 W. L. Marshall and E. Franck, Ion product of water substance, 0–1000 C, 1–10,000 bars New International Formulation and its background, *J. Phys. Chem. Ref. Data*, 1981, **10**(2), 295–304.
52 M. Cavali, N. L. Junior, J. D. de Sena, A. L. Woiciechowski, C. R. Soccol, P. Belli Filho, *et al.*, A review on hydrothermal carbonization of potential biomass wastes, characterization and environmental applications of hydrochar, and biorefinery perspectives of the process, *Sci. Total Environ.*, 2023, **857**, 159627.
53 M. Wu, G. Lin, D. Chen, G. Wang, D. He, S. Feng, *et al.*, Sol-hydrothermal synthesis and hydrothermally structural evolution of nanocrystal titanium dioxide, *Chem. Mater.*, 2002, **14**(5), 1974–1980.
54 M. Lucian, M. Volpe, L. Gao, G. Piro, J. L. Goldfarb and L. Fiori, Impact of hydrothermal carbonization conditions on the formation of hydrochars and secondary chars from the organic fraction of municipal solid waste, *Fuel*, 2018, **233**, 257–268.
55 D. Xu, G. Lin, L. Liu, Y. Wang, Z. Jing and S. Wang, Comprehensive evaluation on product characteristics of fast hydrothermal liquefaction of sewage sludge at different temperatures, *Energy*, 2018, **159**, 686–695.
56 S. Hongthong, S. Raikova, H. S. Leese and C. J. Chuck, Co-processing of common plastics with pistachio hulls via hydrothermal liquefaction, *Waste Manag.*, 2020, **102**, 351–361.
57 O. Okoligwe, T. Radu, M. C. Leaper and J. L. Wagner, Characterization of municipal solid waste residues for hydrothermal liquefaction into liquid transportation fuels, *Waste Manage.*, 2022, **140**, 133–142.
58 B. Guo, B. Yang, Y. Su, S. Zhang, U. Hornung and N. Dahmen, Screening and optimization of microalgae biomass and plastic material coprocessing by hydrothermal liquefaction, *ACS ES&T Eng.*, 2021, **2**(1), 65–77.
59 Y. Guo, X. Liu, M. U. Azmat, W. Xu, J. Ren, Y. Wang, *et al.*, Hydrogen production by aqueous-phase reforming of glycerol over Ni-B catalysts, *Int. J. Hydrogen Energy*, 2012, **37**(1), 227–234.
60 S. Shekoohiyan, A. Sajadi, G. Moussavi and M. Heidari, Hydrothermal carbonization of plastic wastes and effect of influential parameters on performance and challenges: a review, *Int. J. Environ. Sci. Technol.*, 2025, 1–42.
61 D. Serrano, J. Aguado, G. Vicente and N. Sánchez, Effects of hydrogen-donating solvents on the thermal degradation of HDPE, *J. Anal. Appl. Pyrolysis*, 2007, **78**(1), 194–199.
62 A. A. Peterson, F. Vogel, R. P. Lachance, M. Fröling, Jr M. J. Antal and J. W. Tester, Thermochemical biofuel production in hydrothermal media: a review of sub-and supercritical water technologies, *Energy Environ. Sci.*, 2008, **1**(1), 32–65.
63 D. Chiaramonti, M. Prussi, M. Buffi, A. M. Rizzo and L. Pari, Review and experimental study on pyrolysis and hydrothermal liquefaction of microalgae for biofuel production, *Appl. Energy*, 2017, **185**, 963–972.
64 H. B. Sharma, A. K. Sarmah and B. Dubey, Hydrothermal carbonization of renewable waste biomass for solid biofuel production: A discussion on process mechanism, the influence of process parameters, environmental performance and fuel properties of hydrochar, *Renewable Sustainable Energy Rev.*, 2020, **123**, 109761.
65 F. Wang, J. Wang, C. Gu, Y. Han, S. Zan and S. Wu, Effects of process water recirculation on solid and liquid products from hydrothermal carbonization of Laminaria, *Bioresour. Technol.*, 2019, **292**, 121996.
66 Hydrochar production through co-hydrothermal carbonization of water hyacinth and plastic waste, *IOP Conference Series: Earth and Environmental Science*, ed. M. Ong, S. Nomanbhay, C. Rosman, T. Yusaf and A. Silitonga, IOP Publishing, 2024.
67 R. Darzi, Y. Dubowski and R. Posmanik, Hydrothermal processing of polyethylene-terephthalate and nylon-6 mixture as a plastic waste upcycling treatment: A comprehensive multi-phase analysis, *Waste Manage.*, 2022, **143**, 223–231.
68 J. Poerschmann, B. Weiner, S. Woszidlo, R. Koehler and F.-D. Kopinke, Hydrothermal carbonization of poly (vinyl chloride), *Chemosphere*, 2015, **119**, 682–689.
69 N. Kaewtrakulchai, S. Chanpee, S. Jadsadajerm, S. Wongrerkdee, K. Manatura and A. Eiad-Ua, Co-hydrothermal carbonization of polystyrene waste and maize stover combined with KOH activation to develop nanoporous carbon as catalyst support for catalytic hydrotreating of palm oil, *Carbon Resour. Convers.*, 2024, **7**(4), 100231.
70 M. A. Uddin, T. Bhaskar, T. Kusaba, K. Hamano, A. Muto and Y. Sakata, Debromination of flame retardant high impact polystyrene (HIPS-Br) by hydrothermal treatment and recovery of bromine free plastics, *Green Chem.*, 2003, **5**(2), 260–263.
71 A. Gallifuoco, L. Taglieri, F. Scimia, A. A. Papa and G. Di Giacomo, Hydrothermal carbonization of Biomass: New experimental procedures for improving the industrial Processes, *Bioresour. Technol.*, 2017, **244**, 160–165.
72 D. Gupta, S. Mahajani and A. Garg, Effect of hydrothermal carbonization as pretreatment on energy recovery from food and paper wastes, *Bioresour. Technol.*, 2019, **285**, 121329.
73 C. Wang, X. Zhang, L. Wang, G. Liu and G. Boczkaj, Valorization of waste plastics to a novel metal-organic framework derived cobalt/carbon nanocatalyst as peroxymonosulfate activator for antibiotics degradation, *J. Cleaner Prod.*, 2025, **486**, 144539.
74 A. D. Tripathi, P. K. Mishra, K. K. Darani, A. Agarwal and V. Paul, Hydrothermal treatment of lignocellulose waste

for the production of polyhydroxyalkanoates copolymer with potential application in food packaging, *Trends Food Sci. Technol.*, 2022, **123**, 233–250.

75 R. X. Yang, K. Jan, C. T. Chen, W. T. Chen and K. C. W. Wu, Thermochemical conversion of plastic waste into fuels, chemicals, and value-added materials: a critical review and outlooks, *ChemSusChem*, 2022, **15**(11), e202200171.

76 M. J. Sheikhdavoodi, M. Almassi, M. Ebrahimi-Nik, A. Kruse and H. Bahrami, Gasification of sugarcane bagasse in supercritical water; evaluation of alkali catalysts for maximum hydrogen production, *J. Energy Inst.*, 2015, **88**(4), 450–458.

77 S. Nanda, S. N. Reddy, D. V. N. Vo, B. N. Sahoo and J. A. Kozinski, Catalytic gasification of wheat straw in hot compressed (subcritical and supercritical) water for hydrogen production, *Energy Sci. Eng.*, 2018, **6**(5), 448–459.

78 T. Pairojpiriyakul, E. Croiset, K. Kiatkittipong, W. Kiatkittipong, A. Arpornwichanop and S. Assabumrungrat, Catalytic reforming of glycerol in supercritical water with nickel-based catalysts, *Int. J. Hydrogen Energy*, 2014, **39**(27), 14739–14750.

79 J. Watson, Y. Zhang, B. Si, W.-T. Chen and R. De Souza, Gasification of biowaste: A critical review and outlooks, *Renewable Sustainable Energy Rev.*, 2018, **83**, 1–17.

80 L. Tiong, M. Komiyama, Y. Uemura and T. T. Nguyen, Catalytic supercritical water gasification of microalgae: Comparison of Chlorella vulgaris and Scenedesmus quadricauda, *J. Supercrit. Fluids*, 2016, **107**, 408–413.

81 C. Zhu, L. Guo, H. Jin, Z. Ou, W. Wei and J. Huang, Gasification of guaiacol in supercritical water: detailed reaction pathway and mechanisms, *Int. J. Hydrogen Energy*, 2018, **43**(31), 14078–14086.

82 M. Osada, T. Sato, M. Watanabe, T. Adschiri and K. Arai, Low-temperature catalytic gasification of lignin and cellulose with a ruthenium catalyst in supercritical water, *Energy Fuels*, 2004, **18**(2), 327–333.

83 D. Tang, X. Huang, W. Tang and Y. Jin, Lignin-to-chemicals: Application of catalytic hydrogenolysis of lignin to produce phenols and terephthalic acid via metal-based catalysts, *Int. J. Biol. Macromol.*, 2021, **190**, 72–85.

84 T. Yoshikawa, T. Umezawa, Y. Nakasaka and T. Masuda, Conversion of alkylphenol to phenol via transalkylation using zeolite catalysts, *Catal. Today*, 2020, **347**, 110–114.

85 Z.-X. Xu, H. Song, P.-J. Li, Z.-X. He, Q. Wang, K. Wang, *et al.*, Hydrothermal carbonization of sewage sludge: Effect of aqueous phase recycling, *Chem. Eng. J.*, 2020, **387**, 123410.

86 E. Danso-Boateng, A. Mohammed, G. Sander, A. Wheatley, E. Nyktari and I. C. Usen, Production and characterisation of adsorbents synthesised by hydrothermal carbonisation of biomass wastes, *SN Appl. Sci.*, 2021, **3**, 1–19.

87 S. Venna, H. B. Sharma, P. H. P. Reddy, S. Chowdhury and B. K. Dubey, Landfill leachate as an alternative moisture source for hydrothermal carbonization of municipal solid wastes to solid biofuels, *Bioresour. Technol.*, 2021, **320**, 124410.

88 P. Phuthongkhao, K. Phasin, P. Boonma, R. Khunphonoi, E. Kanchanatip, T. Suwannaruang, *et al.*, Preparation and characterization of hydrothermally processed carbonaceous hydrochar from pulp and paper sludge waste, *Biomass Convers. Biorefin.*, 2024, **14**(14), 15493–15510.

89 C. A. Che, K. M. Van Geem and P. M. Heynderickx, Enhancing sustainable waste management: Hydrothermal carbonization of polyethylene terephthalate and polystyrene plastics for energy recovery, *Sci. Total Environ.*, 2024, **946**, 174110.